Inferno Worlds

Ridden - Harper, A.

Citation

Ridden - Harper, A. (2018, November 21). *Inferno Worlds*. Retrieved from https://hdl.handle.net/1887/67080

Author: Ridden, - Harper A.
Title: Inferno Worlds
Issue Date: 2018-11-21

5 Search for gas from the disintegrating rocky exoplanet K2-22b

Based on:
Ridden-Harper, A. R.; Snellen, I. A. G.; Keller, C. U.; P. Mollière, submitted to A&A

Context. The red dwarf star K2-22 is transited every 9.14 hours by an object which is best explained by being a disintegrating rocky exoplanet featuring a variable comet-like dust tail. While the dust is thought to dominate the transit light curve, gas is also expected to be present, either from being directly evaporated off the planet or by being produced by the sublimation of dust particles in the tail.
Aims. Both ionized calcium and sodium have large cross-sections, and although present at low abundance, exhibit the strongest atomic absorption features in comets. We therefore identify these species also as the most promising tracers of circumplanetary gas in evaporating rocky exoplanets and search for them in the tail of K2-22 b to constrain the gas-loss and sublimation processes in this enigmatic object.
Methods. We observed four transits of K2-22 b with X-shooter on ESO's Very Large Telescope to obtain time-series of intermediate-resolution (R $\sim$ 11400) spectra. Our analysis focused on the two sodium D lines (588.995 nm and 589.592 nm) and the Ca^+ triplet (849.802 nm, 854.209 nm and 866.214 nm). The stellar calcium and sodium absorption is removed using the out-of-transit spectra. Planet-related absorption is searched for in the velocity rest frame of the planet, which changes from approximately -66 to +66 km s^{-1} during the transit.
Results. We reached 5σ upper-limits on the tail's sodium and ionized calcium absorption of 9% and 1.4%, respectively. Assuming their mass fractions to be similar to those in the Earth's crust, these limits correspond to scenarios in which only 0.01% and 0.3% of the transiting dust is sublimated and observed as absorbing gas. However, this assumes the gas to be co-moving with the planet. We show that for the high irradiation environment of K2-22 b, sodium and ionized calcium could be quickly accelerated to 100s of km s^{-1} due to radiation pressure and entrainment by the stellar wind, making them much more difficult to detect. No evidence for such possibly broad and blue-shifted signals are seen in our data.
Conclusions. Future observations aimed at observing circumplanetary gas should take into account the possible broad and blue-shifted velocity field of atomic and ionized species.

5.1 Introduction

The NASA Kepler and K2 space missions have unveiled a new class of stars which are transited in short regular intervals of a day or less by objects that are best explained as disintegrating, rocky planets. They produce light curves that randomly vary in depth and shape (typically at $<2\%$) from one orbit to the next, showing features attributed to dust tails, such as forward scattering peaks and asymmetric transit profiles (e.g. Rappaport et al. 2012; Sanchis-Ojeda et al. 2015). During some orbits, the transit can apparently be absent, implying that the transiting parent bodies themselves are too small to be detected, in line with the requirement of low surface gravities to allow a dust-tail to be launched from a planetary surface. A proposed mechanism for this mass-loss is a thermally driven hydrodynamic outflow that may be punctuated by volcanic eruptions (Perez-Becker & Chiang 2013). The composition of the dust likely reflects the composition of the planet, making them excellent targets to study their surface geology. For instance, mass loss and dust composition can be constrained by comparing dust-tail models to transit light curves (Rappaport et al. 2012, 2014; Brogi et al. 2012; Budaj 2013; van Lieshout et al. 2014; Sanchis-Ojeda et al. 2015; van Lieshout et al. 2016, Chapters 3 & 4), and wavelength dependent dust extinction models to spectrophotometric observations (e.g. Croll et al. 2014; Murgas 2013; Bochinski et al. 2015; Alonso et al. 2016).

However, potentially much stronger constraints on the underlying physical mechanisms of mass-loss and the composition of the lost material can be derived by observing the gas that is expected to be evaporated directly from the planet or produced by the sublimation of dust particles in the tail. No such observations yet exist except for the more exotic object transiting the white dwarf WD 1145+017, which appears to have several clumps of closely-orbiting material (Vanderburg et al. 2015; Rappaport et al. 2016). Redfield et al. (2017) observed this system with KECK/HIRES and VLT/X-shooter at five epochs over the course of a year and detected varying circumstellar absorption in more than 250 lines from 14 different atomic or ionized species (O I, Na I, Mg I, Al I, Ca I, Ca II, Ti I, Ti II, Cr II, Mn II, Fe I, Fe II, Ni I, and Ni II).

K2-22 b is one of the four disintegrating planet systems known to date, and is the most promising for detecting gas due to its relative brightness (R=15.01; Rappaport et al. 2012, 2014; Sanchis-Ojeda et al. 2015; Vanderburg et al. 2015). Its host star is an M dwarf ($T_{\rm eff}$ = 3830 K) that has a fainter (R = 18.79) M-dwarf companion ($T_{\rm eff}$ = 3290 K) approximately 2 arcsec away. It has an orbital period of 9.146 hours and produces transit depths that vary from approximately $\lesssim$0.14 to 1.3%, with a mean depth of 0.55%. The minimum transit depth implies an upper-limit on the size of the disintegrating hard-body planet of 2.5 $R_\oplus$, assuming a stellar radius of 0.57 $R_\odot$ (Sanchis-Ojeda et al. 2015).

In contrast to the other known members of this class of object, it appears to exhibit a leading tail producing a large forward scattering peak at egress (Sanchis-Ojeda et al. 2015). This is possible for dust particles that experience a radiation pressure force to stellar gravitational force ratio (β) of $\lesssim 0.02$. Such particles could either have radii $\lesssim$0.1 μm or $\gtrsim$ 1 μm. In contrast, the post-transit forward scattering bump requires particle sizes of approximately 0.5 μm.

A wavelength dependence in transit depth has been observed on at least one occasion (Sanchis-Ojeda et al. 2015), which allowed the Angstrom exponent, α, to be computed, which is defined as $-d\ln\sigma/d\ln\lambda$, where σ is the effective extinction cross section and λ is the wavelength. It indicates a non-steep power-law dust size distribution with a maximum size of approximately 0.5 μm. Considering all of these particle size constraints, Sanchis-Ojeda et al. (2015) conclude that a large fraction of particles must have sizes of approximately 1 μm. Assuming a high-Z dust composition, they estimate a mass-loss rate of approximately 2×10^{11} g s^{-1}.

In this paper we report on a search for sodium and ionized calcium in intermediate resolution spectroscopic time-series data from VLT/X-shooter, focusing on the sodium D lines and the ionized calcium infrared triplet lines. These species and lines were detected in WD 1145+017 by Redfield et al. (2017), which is expected due to their low sublimation temperatures (e.g. Haynes 2011), likely presence in terrestrial planet compositions and large absorption cross-sections (e.g. Mura et al. 2011). This paper is structured as follows: Section 5.2 describes our observational data, Sections 5.3 and 5.4 describe our methods, Section 5.5 presents and discusses our results and Section 5.6 concludes.

5.2 Observational data

We observed transits of the rocky disintegrating planet K2-22 b on the nights of March 18 & April 4, 2017, and March 10 & March, 18, 2018 with X-shooter (Vernet et al. 2011), installed at the Cassegrain focus of ESO's Very Large Telescope Telescope (VLT) at the Paranal Observatory under program ID 098.C-0581(A) (PI:Ridden-Harper). The three-arm configuration of X-shooter, ultraviolet-blue (UVB), visual-red (VIS) and near-infrared (NIR), allows it to quasi-simultaneously observe the spectral range of $300 - 1500$ nm.

These observations were carried out in nodding mode (in an ABBA pattern) with a nod-throw length of 4 arcsec along the slit. During the three hours of observations on each night, 26 individual exposures of 213 seconds were obtained in the VIS arm. The observing dates, transit timing, exposure times and orbital phase coverage are shown in Table 5.1. We used slit widths in the UVB, VIS and NIR arms of 0.5, 0.7 and 0.4 arcsec, which resulted in resolving powers of R $\approx$ 9700, 11400 and 11600, respectively.

X-shooter does not have an atmospheric dispersion corrector (ADC). Therefore after every hour of observing the target was re-acquired and the slit was aligned again to the parallactic angle to minimize slit-losses. The observations were reduced using the standard nodding mode recipes from the X-shooter Common Pipeline Library (CPL) [1]. To enable sky background subtraction, every two exposures (AB or BA) were combined, resulting in 13 1D wavelength-calibrated spectra.

The last four spectra of Night 1 were contaminated by the faint M-dwarf companion of K2-22 that moved into the slit. Due to the apparent difference in spectral type between the target and the companion, the observed depth of the stellar absorption lines changes, making accurate relative spectrophotometry impossible. We therefore excluded this night from the analysis.

5.3 Analyses

Our analyses focused on the two sodium D lines (588.995 nm and 589.592 nm) and the Ca^+ near-infrared triplet (849.802 nm, 854.209 nm and 866.214 nm), which were both captured by the VIS arm of X-shooter. The observed spectral regions are dominated mainly by stellar and some telluric lines. Both the reflex motion of the star around the system's barycenter[2] and the change in the radial component of the velocity of the observatory towards the star are so small that they can be considered to be non-variable, as well as the position (but not the strength) of the telluric lines. In contrast, the orbital velocity of the planet is large, leading to a change in the radial component during transit from approximately −66 to +66 km s^{-1}. The resulting Doppler shift of the planetary lines can be used to separate them from the stellar and telluric features. The analysis was carried out as in Chapter 2, but is summarised below for completeness. It is comprised of the following steps, and is near identical for the investigation of both the calcium and sodium lines.

1. Normalization to a common flux level: Variable slit losses and atmospheric scattering cause the spectra to have different flux levels. This is corrected by division through their median value for a wavelength range close to the targeted lines (to avoid offsets due to variable low-frequency trends in the spectra). This normalization is possible because transmission spectroscopy depends on the relative change in flux as a function of wavelength and is therefore not an absolute measurement.

---

[1] Available at: https://www.eso.org/sci/software/pipelines/xshooter/

[2] Sanchis-Ojeda et al. (2015) did not detect any radial velocity variations in the spectrum of K2-22 (accurate to ± 0.3 km s^{-1}).

Table 5.1: Details of the observations. The orbital phases of K2-22 b are based on the orbital parameters derived by Sanchis-Ojeda et al. (2015).

data set	Night 1	Night 2	Night 3	Night 4
date (UTC)	19 March 2017	4 April 2017	11 March 2018	19 March 2018
start phase	0.832	0.833	0.856	0.806
end phase	0.150	0.147	0.178	0.122
cadence (s)	419.3	414.3	423.2	416.6
exposure time (s)	213[†]	213[†]	213[†]	213[†]
observation start (UTC)	02:00:34	02:08:22	03:54:45	03:30:56
transit start* (UTC)	03:00:31	03:08:45	04:41:20	04:45:12
mid-transit time* (UTC)	03:24:31	03:32:45	05:05:20	05:09:12
transit end* (UTC)	03:48:31	03:56:45	05:29:20	05:33:12
observation end (UTC)	04:55:18	05:01:00	06:51:06	06:24:31
Nr. spectra pre-transit	5	5	4	6
Nr. spectra in transit	4	4	4	4
Nr. spectra post-transit	4	4	5	3
total Nr. of spectra	13	13	13	13
Na D line region S/n.[1]				
average S/n. per spectrum	30.79	38.44	35.65	27.92
total S/n	61.58	76.89	71.30	55.84
Ca^+ triplet region S/n.[2]				
average S/n. per spectrum	101.17	111.27	113.65	111.34
total S/n	202.33	222.54	227.29	222.69

* The transit times are barycentric adjusted to be as measured at the observatory.

† Except for the last two spectra which have exposure times of 211 s.

1 and 2: derived from the residuals after dividing by the mean spectrum of the featureless regions 5961.0 Å − 5965.2 Å and 8584.8 Å − 8591.8 Å, respectively.

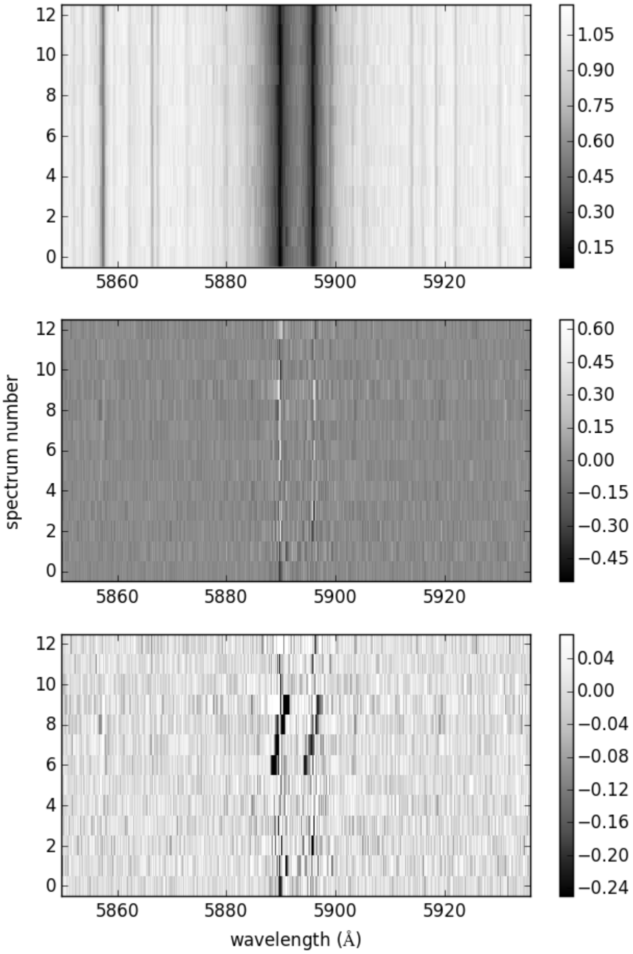

Figure 5.1: A visual representation of the processing steps as described in Section 5.3. This figure shows the data of Night 4, but the other nights are very similar. The vertical axis of each matrix represents the sequence number of the observed spectrum. The first panel shows the data around the sodium D lines after normalization and alignment in Step 2. The second panel shows the residual matrix after dividing through the average star spectrum and subtracting the mean (Step 4). The bottom panel shows the data after injecting an artificial planet signal before Step 2 that absorbs 50% of the stellar flux. The injected planet signal can be seen as a diagonal trace from spectrum number 6 to 9, resulting from the change in the radial component of the planet orbital velocity during transit.

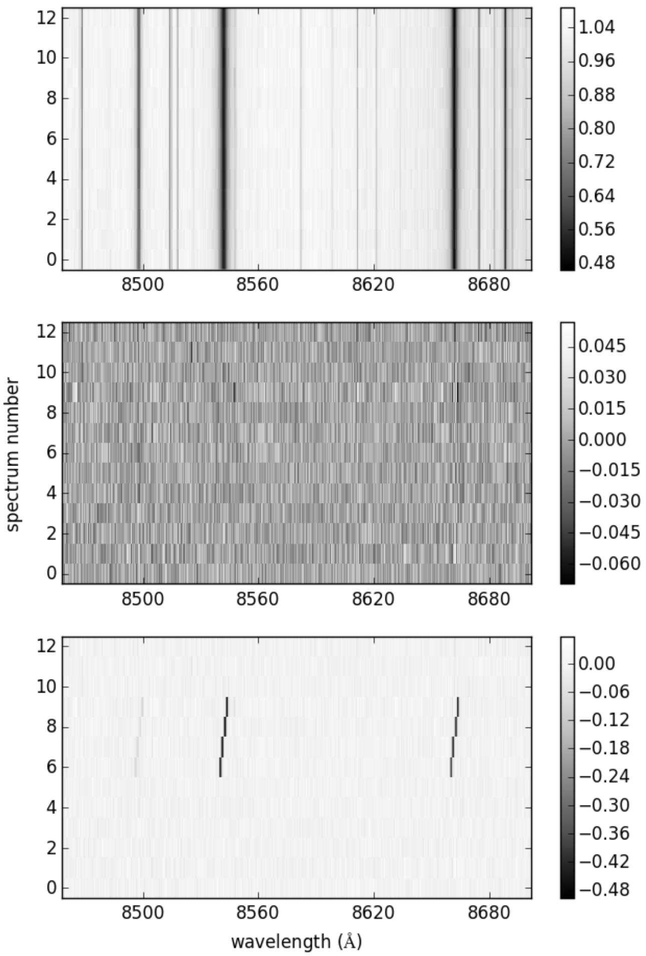

Figure 5.2: Same as Fig. 5.1 but for the ionized calcium near-infrared triplet.

2. Alignment of the spectra: Due to instrumental instability, the wavelength solution is prone to changes at a sub-pixel level. Since the absolute wavelength solution is not relevant for our analysis, the positions of strong spectral lines are fitted in each spectrum and used to shift all spectra to a common wavelength frame.

3. Removal of cosmic rays: Cosmic rays were removed by searching for 5σ outliers and replacing them with a value interpolated from a linear fit to the other spectra at the affected wavelength position.

4. Removal of stellar and telluric lines: All stationary spectral components in the spectra were removed by dividing every pixel in a spectrum by the mean value of the out-of-transit spectra at that wavelength position during the night. Since the Doppler shift of the planet lines changes by approximately 5 pixels during the transit, this procedure has only a limited effect on potential planet lines.

5. Down-weighting of noisy parts of the spectrum: Noisy parts of the spectrum, e.g. in the center of strong absorption lines or telluric lines can have a significant effect on the cross-correlation functions. Therefore the flux points at each wavelength are weighted down according to the signal-to-noise ratio as a function of wavelength, derived from the standard deviation of the residual spectra at each wavelength position. This function was scaled differently for each spectrum, such that the wavelengths where the planet's signal should be located were not changed (i.e. scaled by a factor of one). This preserved the fractional absorption of the injected planet signal relative to the stellar spectrum.

6. Combination of individual lines. The data from the three individual ionized calcium lines were combined after weighting by the line strengths. The two sodium lines were combined in the same way.

7. Combining the individual nights. We shifted the line-combined spectra to the planet rest frame using the transit timing parameters from Sanchis-Ojeda et al. (2015), and subsequently summed over all spectra taken during transit. These 1D spectra were subsequently combined for the different nights, weighted by their average signal-to-noise ratio during the night (See Table 5.1.

In many other data sets, variable telluric lines cause structure in the residual spectra that can be removed with a principle component analysis (PCA), which involves decomposing the data into principle components and removing the dominant structures by subtracting the first few dominant components (e.g. Chapter

2). However, the telluric lines did not significantly vary during these observations so PCA did not improve the recovery of our injected signals (see Section 5.4) and was not applied.

Visual representations of the data analysis process for both the Na D doublet and the Ca^+ triplet are shown in Figs. 5.1 and 5.2, respectively.

5.4 Synthetic planet signal injection

Synthetic planet signals were injected after stage two of the analysis process (see above) to examine to what extent the analysis affects a potential planet signal and to assess the overall sensitivity of the data. The data with the artificial signals were treated in the same way as the unaltered data sets.

We injected a simple model of the Ca^+ infrared triplet and the two Na D lines with relative line intensities approximated using Eq. 1 in Sharp & Burrows (2007), for now ignoring terms that relate to the energy level population (e.g. temperature and partition function). This means that the degeneracy factor, g, is not included in these calculations, because it is part of the level population terms. This approach assumes that the population of Na atoms is in the ground state and that all of the Ca^+ ions are in the lower state of the triplet transition studied here. For Ca^+ this is not the case, and we will adjust the mass limits derived for this ion using its expected population statistics in Section 5.5.1. We took the quantum parameters that describe the line transitions from the National Institute of Standards and Technology (NIST) Atomic Spectra Database (Kramida et al. 2018). The values and references are shown in Table 5.2. For the sodium D lines at 5889.95 Å and 5895.92 Å, we derive a line ratio of 2.0. For the ionized calcium triplet lines at 8498.02 Å 8542.09 Å and 8662.14 Å, the relative line strengths derived are 0.167, 1.000, 0.829, respectively.

During an exposure of 213 seconds, the radial component of the orbital velocity of the planet changes by approximately 7.5 km s^{-1}. Since each time two exposures are combined to generate one spectrum, this results in a convolution with a boxcar function with a width of 15 km s^{-1}, comparable to the instrumental resolution. The planet model spectrum was Doppler shifted to the appropriate planet velocity, assuming a circular orbit (Sanchis-Ojeda et al. 2015), and injected according to

$$F'(\lambda) = [1 - C \times F_{model}(\lambda, v_{rad})]F_{obs}(\lambda) \tag{5.1}$$

where $F_{obs}(\lambda)$ is the observed spectrum, $F_{model}(\lambda, v_{rad})$ is the Doppler-shifted model spectrum, with C as a scaling parameter that determines the amplitude of strongest line, and $F'(\lambda)$ is the resulting spectrum after injecting the synthetic planet spectrum. To determine the upper-limits in the strength of the ionized calcium and sodium lines, the scaling parameter C was varied to reach a signal five times larger than the noise in the combined 1D planet-rest-frame spectrum.

5.5 Results and discussion

No significant signal from neither sodium nor ionized calcium was detected. Injection of synthetic planet signals indicate that 5σ upper-limits were reached when the strength of the strongest line (C in Equation 5.1) was set to 9% and 1.4% for the sodium D doublet and the Ca^+ triplet, respectively. We conservatively quote 5σ limits because a systematic noise is present at the 3σ level that was challenging to properly account for.

The combined (over individual lines and over nights $2-4$) transmission spectrum as a function of orbital phase is shown in Figs. 5.3 and 5.4 for Na and Ca^+, respectively. Nearest-pixel interpolation was used, necessary since observations at different nights were not performed at identical orbital phases. The panels show the data without injected signals (top), with injected signals at 5σ (middle), and at 10σ (bottom). The injected signal of sodium is significantly less pronounced around mid-transit, because it temporarily overlaps with the cores of the noisy stellar sodium absorption. These spectra are weighed down accordingly for the construction of the final 1D transmission spectrum.

The final 1D-spectra per night, and those combined over nights $2-4$ are shown in Figs. 5.5 and 5.6 (with and without the injected signals) for the Na D lines and the Ca^+ triplet, respectively. The right panels are those binned by 0.8Å to 40 km s^{-1}. Combining the two Na lines and three Ca^+ lines results in neighbouring lines being included in the combined 1D spectrum (e.g. for Na, the features at $\pm$ 285 km s^{-1}).

5.5.1 Instantaneous gas-mass limits

To estimate what the observed limits mean in terms of Ca^+, Na, and total gas mass-loss limits, we used the following equation for absorption line strength as described in Savage & Sembach (1991):

$$\tau(v) = \frac{\pi e^2}{m_e c} f\lambda N(v) = 2.654 \times 10^{-15} f\lambda N(v) \tag{5.2}$$

where f is the transition oscillator strength, λ is the wavelength in Angstroms, and $N(v)$ is the integral normalized column density per unit velocity in atoms cm^{-2} (km $\mathrm{s}^{-1})^{-1}$. We assumed that lines from the gas would be too narrow to resolve at our instrument resolution of R $\sim$ 11400 so our column density profile, $N(v)$, only accounted for the line's natural width. This was done by setting the

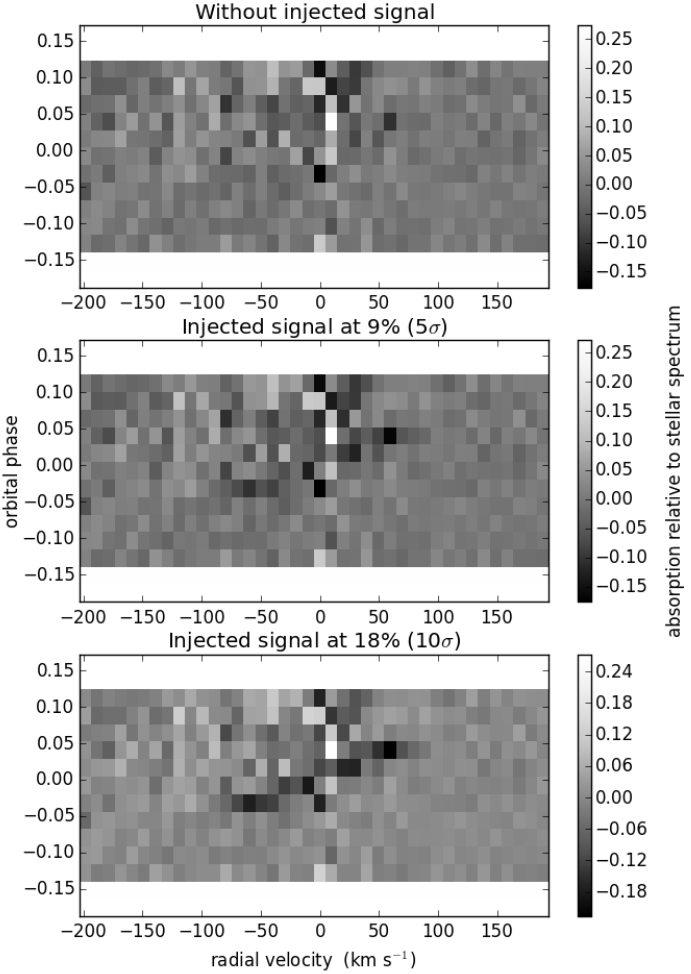

Figure 5.3: Planet Na D transmission spectrum combined from nights $2-4$ as a function of orbital phase (vertical axis) and radial velocity in the planet rest frame, with no injected signal (top), a 9% injected signal corresponding to a 5σ limit (middle) and an 18% injected signal (bottom).

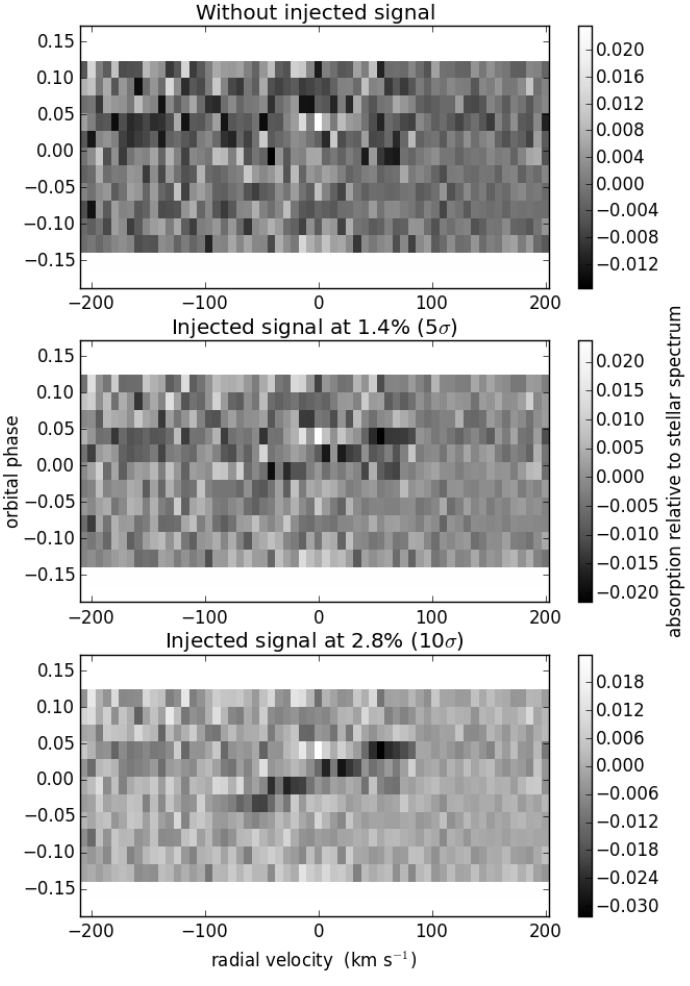

Figure 5.4: Same as Fig. 5.3, except for the calcium near infrared triplet. The middle panel shows an injected signal of 1.4% and the bottom panel shows an injected signal of 2.8%.

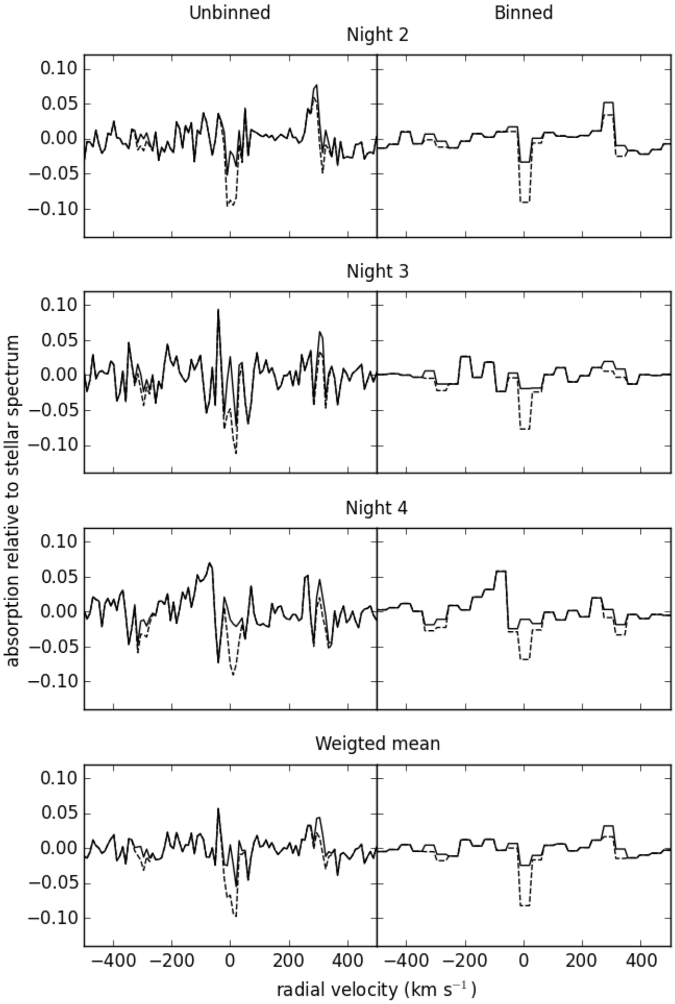

Figure 5.5: Planet transmission spectrum of the combined sodium D lines for Nights 2 to 4 and their combination (bottom panels). The left and right panels show the unbinned and binned (at 0.8Å or 40 km s^{-1}) data, respectively. The solid and dashed lines indicated the non-injected and injected data (at a 9% depth) respectively.

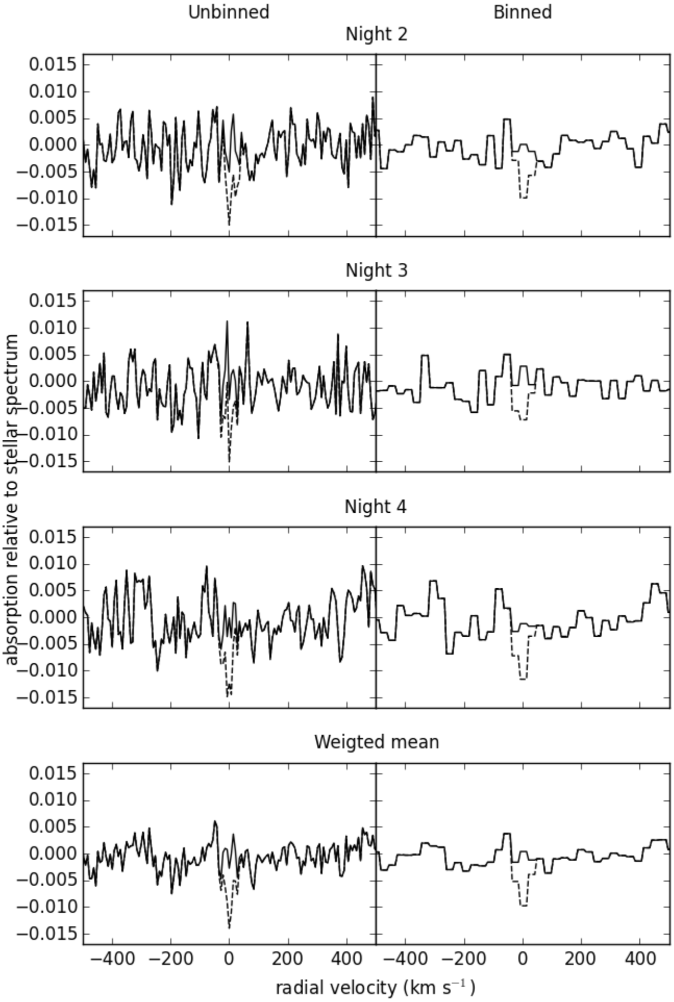

Figure 5.6: Same as Fig. 5.5 but for the ionized calcium near infrared triplet with an injected signal strength of 1.4% relative to the stellar spectrum.

Table 5.2: Spectral line transition parameters.

Spectral line (Å)	f_{ik}	A_{ki} (s^{-1})	Normalisation factor†	reference
Na				
5889.95	0.641	6.16×10^{7}	112.03	1
5895.92	0.320	6.14×10^{7}	112.28	1
Ca^{+}				
8498.02	0.0120	1.11×10^{6}	4309.09	2
8542.09	0.072	9.9×10^{6}	480.65	2
8662.14	0.0597	1.06×10^{7}	442.69	2

† Derived quantity.
Reference 1: Juncar et al. (1981).
Reference 1: Edlén & Risberg (1956).
Values retrieved from NIST Atomic Spectra Database (Kramida et al. 2018).

full-width-at-half-maximum (FWHM) of a Lorentzian line profile to the transition's natural line width given in angular frequency units by the Einstein A coefficient (or spontaneous decay rate, Γ). We then numerically integrated the line profile to find the required normalization factor. The parameters that we used are shown in Table 5.2. In reality, there will also be some kinetic broadening in the gas (see also the discussion below). To approximate this without making assumptions about its pressure and temperature, we convolved the optical depth profile with the instrument resolution to broaden the line. This maximized the broadening while minimizing optical thickness effects.

The line intensity profile, $I(\lambda)$, is estimated from the convolved optical depth profile according to

$$I(\lambda) = I_0(\lambda)\exp\left(-\tau(\lambda)\right) \tag{5.3}$$

where $I_0(\lambda)$ is the continuum intensity.

The 5σ upper-limit for sodium corresponds to a 9% absorption depth for the strongest line at 5889.95 Å, which requires an absorbing mass of sodium gas of 3.4×10^{9} g assuming it is optically thin. This implies an upper-limit on the total gas mass of 1.4×10^{11} g, assuming that the dust's composition is the same as that of the Earth's crust.

While we assume that all sodium atoms are in the ground state and therefore can produce the targeted absorption lines, this is not the case for ionized calcium. The targeted lines originate from ions in the meta-stable $3d^2D_{3/2}$ and $3d^2D_{5/2}$ states. To estimate the fraction of calcium II ions in these energy states, we created a simple model consisting of three energy levels: E_0, E_1, and E_2. E_0 is the ground state ($4s^2S_{1/2}$), E_1 is the average of the $3d^2D_{3/2}$ and $3d^2D_{5/2}$ states, and E_2 is the average of the $4p^2p^0_{3/2}$ and $4p^2p^0_{1/2}$ states. Transitions from the E_0 level to the E_2 level produce the H and K lines at 3934Å & 3963Å, while transitions from the E_1 level to the E_2 level produce the near-infrared triplet lines, probed in this study. We also consider the classically forbidden transitions from the E_1 level to the E_0 level, which produce emission at 7291Å and 7324Å.

Spontaneous decay from a high to low energy state occurs at a rate that is proportional to the transition's Einstein A coefficient. Additionally, a transition from a low to high energy state occurs at a rate that is proportional to the rate of photons of energy equal to the energy difference between the states. We calculated the photon rates for the E_0 to E_2 and E_1 to E_2 transitions according to

$$\gamma = \int_{-\infty}^{\infty} F_\nu \left(\frac{R_s}{d}\right)^2 \frac{1}{h\nu} a(\nu) d\nu \tag{5.4}$$

where γ is the rate of photons per second, ν is the frequency, F_ν is the flux as a function of unit frequency, R_s is the radius of the star K2-22, d is the orbital distance of K2-22 b, h is the Planck constant and $a(\nu)$ is the transition's cross-section, assumed to be a Lorenzitan profile of FWHM equal to the transition's natural width. For F_ν we used a PHOENIX model spectrum (Husser et al. 2013) of effective temperature $T_{\rm eff}$ = 3820 K that was normalized such that $\int_{-\infty}^{\infty} F_\nu = \sigma T_{\rm eff}^4$, where σ is the Stefan-Boltzmann constant.

Using these calculated transition rates, the steady state solution of the system was found to have 0.26% of its calcium II ions in the infrared-triplet-forming E_1 state.

For the 5σ upper-limit for Ca^+ of 1.4% absorption of the strongest line at 8542.09 Å, the upper-limits on the mass of Ca^+ gas and the total dust mass are 2.1×10^{12} g and 7.1×10^{13} g, respectively.

5.5.2 Dust and gas mass-loss comparison

The dust mass-loss rate required to produce the observed optical transit depth can be estimated based on the rate at which dust particles pass through the area occulting the host star. Following the method described in Rappaport et al. (2014), Sanchis-Ojeda et al. (2015) estimate K2-22 b's mass-loss rate to be 2×10^{11} g s^{-1}.

We can compare our derived gas-mass upper-limits to the dust mass-loss rate if we assume an appropriate timescale for the absorption by the gas. We take this to be the photo-ionization lifetime of the absorbing species, since they are only able to absorb at the probed transitions until they are photo-ionized. We estimated these lifetimes by scaling the values given by Mura et al. (2011) for CoRoT-7 b to K2-22 b, based on the stellar fluxes and the planet orbital distances. The ionization of Na and Ca^+ requires photons of wavelength less than 240 nm and 104 nm, respectively. The flux at these wavelengths is produced by chromospheric emission and, For M-dwarfs, this flux is typically one to two orders of magnitude less than their flux in the u-band (e.g. Stelzer et al. 2013). To allow for the possibility of high chromospheric emission caused by stellar activity, we conservatively use the Johnson u-band magnitude for this scaling, and find that the u-band flux at K2-22 b is only 27 times larger than what the Sun produces at 1 au distance in the solar system, giving ionization lifetimes of 7.0×10^3 s and 1.2×10^5 s for Na and Ca$^+$, respectively. We neglected the photo-ionization timescale of Ca because it is only $\sim 5.0 \times 10^2$ s. For comparison, the photo-ionization lifetimes of Na and Ca at 1 au in the solar system are 1.9×10^5 s and 1.4×10^4 s, respectively (Fulle et al. 2007; Mura et al. 2011). The photo-ionization lifetime of Ca$^+$ is not well constrained and was estimated by Mura et al. (2011).

From the dust mass-loss rate and photo-ionization lifetimes, we can predict the expected gas column density using

$$M_{gas} = Q\dot{M}_{dust}\tau_{ph} \tag{5.5}$$

where $\dot{M}_{dust}$ is the dust mass-loss rate of K2-22 b, τ_{ph} is the photo-ionization lifetime of the species and Q is the fraction of available dust mass that becomes absorbing gas for a given species. We converted the gas mass into a column density by assuming that the atoms are evenly distributed across the stellar disk. In reality, the gas will probably not cover the entire stellar disk but this is a reasonable assumption because the gas is expected to be optically thin. The expected line strengths as a function of Q are shown in Fig. 5.7 for the sodium D lines and the Ca$^+$ triplet. Our conservative scaling of the photo-ionization timescale means that Q is an upper-limit.

Fig. 5.7 implies that if the gas were co-moving with the planet, we could have expected to detect absorption by Na and Ca$^+$ if only $Q = 0.01\%$ and 0.3% of the available lost mass in dust became absorbing gas, respectively. In contrast, it may well be that all of the dust sublimates and becomes gas ($Q = 1$) and that Q may even be >1 because additional gas may be directly lost from the planet. It is clear that under our simplified assumptions there is no evidence for such a high Q value.

5.5.3 Important Caveats: high velocity gas

Our estimated gas absorptions were based on important assumptions: We assume that the dust particles completely sublimate in the time it takes them to drift across the stellar disk. This is a reasonable assumption because the tail's exponential scale length, l, is estimated to be $0.19 < l < 0.48$ stellar radii (Sanchis-Ojeda et al. 2015). We also assume that the gas has the same orbital velocity as the planet. However, this may not be valid as the gas could be highly accelerated by the stellar wind and radiation pressure, giving a very broad spectral line with gas radial velocities ranging from the planet's radial velocity to 100s of km s^{-1}.

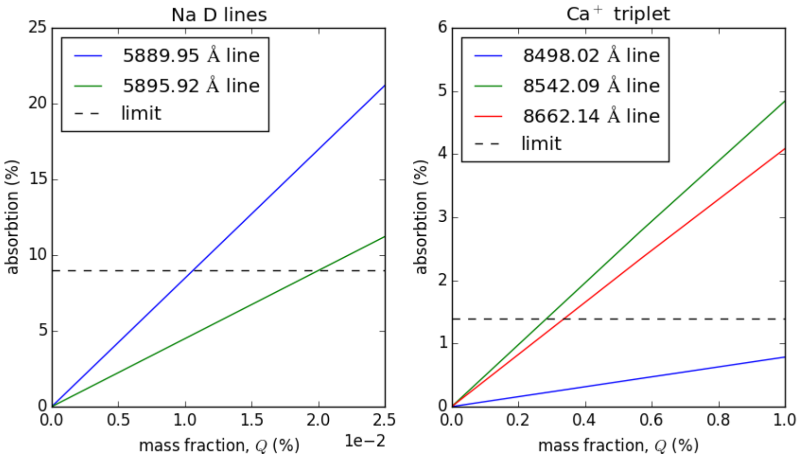

Figure 5.7: Absorption by the Na D lines (left) and the Ca^+ triplet (right) as a function of fraction of available lost mass that becomes absorbing gas, assuming a dust-mass loss rate of 2×10^{11} g s^{-1}, Earth crust abundances and absorption lifetimes equal to the photo-ionization lifetimes of 7.0×10^3 s and 1.2×10^5 s, respectively.

Acceleration of Ca^+ by the stellar wind

In the absence of a strong planetary magnetic field, ionized calcium (Ca^+) will be dragged along by the stellar wind and quickly reach the velocity of the wind, which is typically on the order of a few hundred km s^{-1} (e.g. Johnstone et al. 2015). However, if the planet were to have a magnetic field, it can trap the Ca^+ ions, preventing them from being swept away by the stellar wind. This may explain the potential detection of Ca^+ around 55 Cancri e in Chapter 2.

The MESSENGER spacecraft detected Ca^+ in the exosphere of Mercury, however it was trapped by Mercury's magnetic field. It was detected in a narrow region $2-3$ Mercury radii in the anti-solar direction, exhibiting velocities of hundreds of km s^{-1}. The distribution and velocities of Ca^+ ions is likely due to a combination of magnetospheric convection and centrifugal acceleration (Vervack et al. 2010).

Ionized calcium has also been observed in Sun-grazing comets (e.g Marsden 1967). Additionally, Gulyaev & Shcheglov (2001) detected Ca^+ at distances of $5-20$ $R_\odot$ from the Sun and found that it had radial velocities of $170-280$ km s^{-1}. They propose that the Ca^+ is produced by the sublimation of orbiting interplanetary dust so that its final velocity is a result of its orbital motion and acceleration by the solar wind.

If the Ca^+ ions are swept away by the stellar wind, their spectral lines will be significantly blue shifted and the line width will be broadened from velocities on the order of the planet's radial velocity, to the velocity of the stellar wind. This would strongly hamper the detectability of this gas with the instrumental set-up discussed here.

Stellar radiation pressure

Atoms in an asymmetric photon field will experience a radiation pressure governed by the wavelength-dependent photon density and their absorption cross-sections. If an atom has a radial velocity relative to the photon source, the wavelength-dependency of the absorption cross-section will Doppler-shift accordingly. This can have a large effect e.g. for sodium for which the stellar absorption lines can be very deep. Doppler-shifting these lines significantly can increase the relevant photon flux by an order of magnitude for stellar absorption lines that are 90% deep, causing high accelerations.

Typical accelerations of neutral sodium in the exospheric tail of Mercury are $0.2 - 2$ m s^{-2} (Potter et al. 2007). The final velocity that an accelerated atom can reach depends on the timescale over which it is accelerated, which in the case of neutral atoms equals the photo-ionization lifetime. Cremonese et al. (1997) observed a neutral sodium tail from comet Hale-Bopp when it was at a distance of 1 au, and measured radial velocities of sodium atoms of $60 - 180$ km s^{-1}, along its tail of sky-projected length 31×10^6 km. Similarly, radiation pressure accelerates hydrogen that has escaped from the evaporating atmospheres of the hot Jupiters HD 209458 b and HD 189733 b to velocities of approximately 130 km s^{-1} (e.g. Bourrier & Lecavelier des Etangs 2013).

The final velocity that such atoms reach in a given system is expected to be roughly independent of the distance from the host star, since the acceleration scales as d^{-2}, with d the orbital distance, and the ionization time scale as d^2, the latter counteracting the former.

Comparing the solar spectrum with that of K2-22, using the solar absolute magnitudes from Willmer (2018) and calculating the absolute magnitudes of K2-22 from Sanchis-Ojeda et al. (2015), we find that the optical radiation pressure acting on the neutral sodium atoms at the location of K2-22 b is approximately 150 times higher than for the Earth in the solar system. The stellar u-band flux at K2-22 b is $\sim$30 times larger than on Earth, leading to a shorter ionization time scale by a similar factor. Combining these two effects leads to a maximum velocity of $\sim 150/30 = 5$ times larger than that of sodium tails in the solar system. Note that potential effects of high energy activity such as flares are neglected.

We searched for blueshifted signals of Na and Ca$^+$ using the ratio of the average in-transit to out-of-transit signals in the residual spectra, after removing the stellar and telluric features. Figs. 5.8 and 5.9 show these ratios for Na and Ca$^+$, respectively, which do not exhibit any statistically significant features over the radial velocity range of ± 1000 km s^{-1}. There are a few outlying points but these are only due to the high noise in the cores of the targeted lines.

5.5.4 Alternative interpretations

An alternative explanation for our non-detection is that the planet and dust particles may not have a typical terrestrial planet composition. Furthermore, even if the planet overall does have an expected composition, the dust particles may not directly reflect this. By modelling the light curve of the similar disintegrating planet Kepler-1520 b, van Lieshout et al. (2016) found its dust composition to be consistent with corundum (Al_2O_3), which is somewhat surprising because it is not a major constituent of typical terrestrial planet compositions. They suggest that this may be due to the dust grain formation process favouring the condensation of particular species or the planet's surface being covered in a magma ocean that has been distilled to the point of containing mostly calcium and aluminium oxides. A similar process may be occurring on K2-22 b, reducing the abundance of Na and Ca in the dust particles.

Another potential explanation of our non-detection is that all of our observed transits happened to be during quiescent periods of low mass-loss rates. However, based on the observed transit depth variability, we consider this to be unlikely. It would be beneficial for future spectroscopic observations to be carried out simultaneously with optical photometric observations to allow the contemporaneous mass-loss rate to be estimated.

5.6 Conclusions and future outlook

We observed four transits of the disintegrating rocky exoplanet K2-22 b with X-shooter/VLT to search for absorption by gas that is lost directly by the planet or produced by the sublimation of dust particles in its tail. In particular, we focused on the sodium D line doublet (588.995 nm and 589.592 nm) and the Ca^+ near infrared triplet (849.802 nm, 854.209 nm and 866.214 nm).

We detect no significant Na nor Ca^+ associated with the planet, and derive 5σ upper-limits on their possible absorptions of 9% and 1.4% relative to the stellar continuum, respectively, which points to low gas-loss limits compared to the estimated average dust mass loss derived for this system. We suggest that the probed gases are probably accelerated by the stellar wind and radiation pressure, leading to very broad, blueshifted signals with widths up to 900 km s^{-1}, which would be hard to detect with the instrumental set-up used. We searched for such signals in our data but did not find them.

If the signals from gas-loss are indeed very broad, it may be good to search for them using spectrographs with lower spectral resolution, either using ground-based telescopes utilizing multi-object spectroscopy for calibration, or using the

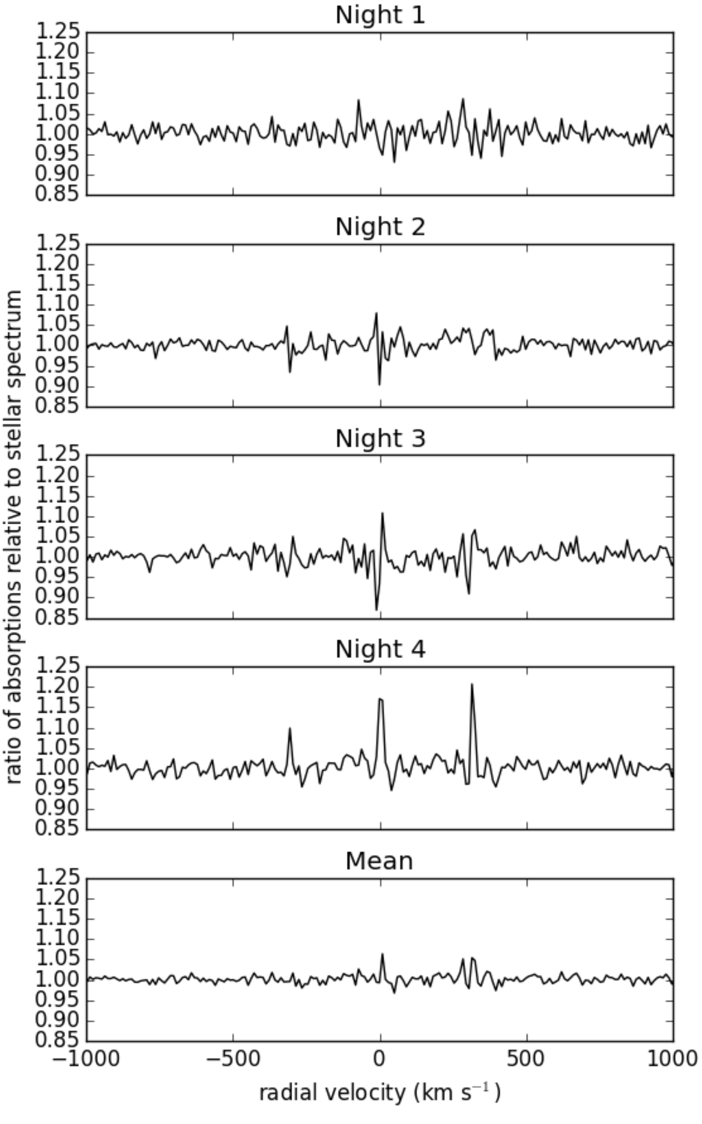

Figure 5.8: Ratio of the average in-transit to out-of-transit signal of blueshifted sodium gas.

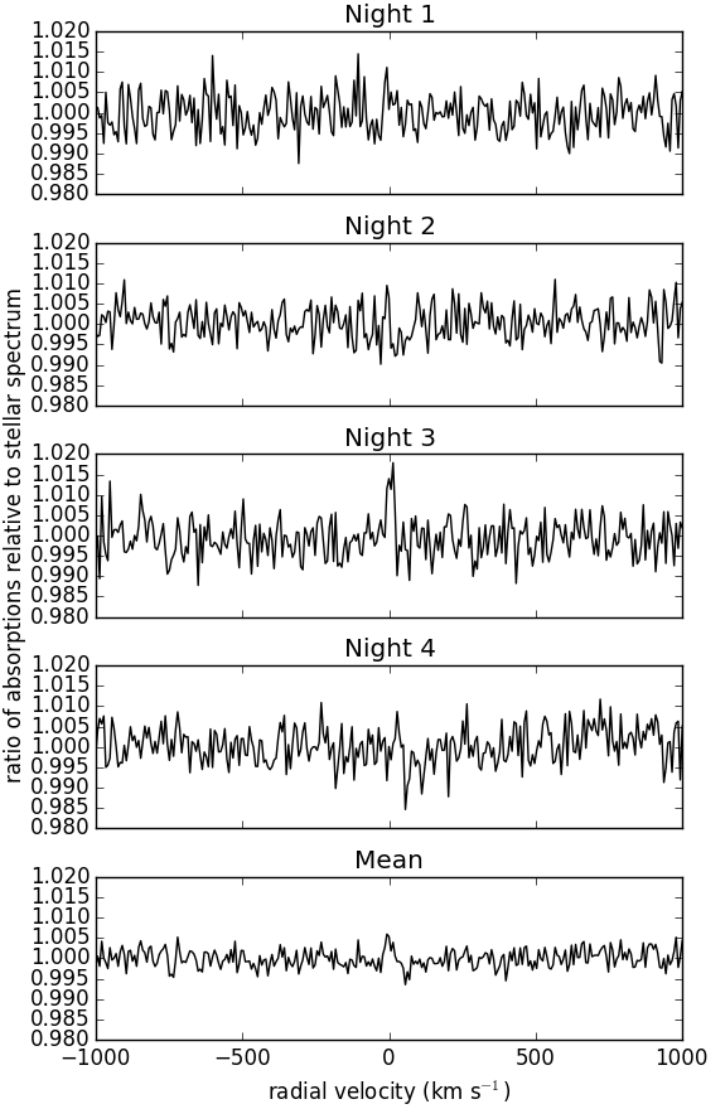

Figure 5.9: Same as Fig. 5.8 except for Ca$^+$ gas.

future JWST – although the sodium D lines are just outside the wavelength range covered by NIRSPEC. In addition, other species such as O, Mg, Ti, Cr, Mn Fe and Ni could be searched for as they were detected in the circumstellar disk of the white dwarf WD 1145+017, which is thought to originate from disintegrating planetesimals (Redfield et al. 2017). While in principle, the combination of multiple species in the transit model would increase the chance of detection – since many lines can be combined, they may all be at a different levels of sensitivity to radiation pressure and acceleration by the stellar wind, making combination more challenging.

Acknowledgements

A. R. R.-H. is grateful to the Planetary and Exoplanetary Science (PEPSci) programme of the Netherlands Organisation for Scientific Research (NWO) for support. I. A. G. S. acknowledges support from an NWO VICI grant (639.043.107), and from the European Research Council under the European Union's Horizon 2020 research and innovation programme under grant agreement No. 694513.

Bibliography

Alonso, R., Rappaport, S., Deeg, H. J., & Palle, E. 2016, A&A, 589, L6

Bochinski, J. J., Haswell, C. A., Marsh, T. R., Dhillon, V. S., & Littlefair, S. P. 2015, ApJ, 800, L21

Bourrier, V. & Lecavelier des Etangs, A. 2013, A&A, 557, A124

Brogi, M., Keller, C. U., de Juan Ovelar, M., et al. 2012, A&A, 545, L5

Budaj, J. 2013, A&A, 557, A72

Cremonese, G., Boehnhardt, H., Crovisier, J., et al. 1997, ApJ, 490, L199

Croll, B., Rappaport, S., DeVore, J., et al. 2014, ApJ, 786, 100

Edlén, B. & Risberg, P. 1956, Ark. Fys. (Stockholm), 10, 553

Fulle, M., Leblanc, F., Harrison, R. A., et al. 2007, ApJ, 661, L93

Gulyaev, R. A. & Shcheglov, P. V. 2001, Physics Uspekhi, 44, 203

Haynes, W. M. 2011, CRC Handbook of Chemistry and Physics, 92nd edn. (CRC Press)

Husser, T.-O., Wende-von Berg, S., Dreizler, S., et al. 2013, A&A, 553, A6

Johnstone, C. P., Güdel, M., Lüftinger, T., Toth, G., & Brott, I. 2015, A&A, 577, A27

Juncar, P., Pinard, J., Hamon, J., & Chartier, A. 1981, Metrologia, 17, 77

Kramida, A., Yu. Ralchenko, Reader, J., & and NIST ASD Team. 2018, NIST Atomic Spectra Database (ver. 5.5.6), [Online]. Available: `https://physics.nist.gov/asd` [2018, June 29]. National Institute of Standards and Technology, Gaithersburg, MD.

Marsden, B. G. 1967, AJ, 72, 1170

Mura, A., Wurz, P., Schneider, J., et al. 2011, Icarus, 211, 1

Murgas, F. 2013, PhD thesis, Departamento de astrofisica, unisersidad de La Laguna

Perez-Becker, D. & Chiang, E. 2013, MNRAS, 433, 2294

Potter, A. E., Killen, R. M., & Morgan, T. H. 2007, Icarus, 186, 571

Rappaport, S., Barclay, T., DeVore, J., et al. 2014, ApJ, 784, 40

Rappaport, S., Gary, B. L., Kaye, T., et al. 2016, MNRAS, 458, 3904

Rappaport, S., Levine, A., Chiang, E., et al. 2012, ApJ, 752, 1

Redfield, S., Farihi, J., Cauley, P. W., et al. 2017, ApJ, 839, 42

Sanchis-Ojeda, R., Rappaport, S., Pallè, E., et al. 2015, ApJ, 812, 112

Savage, B. D. & Sembach, K. R. 1991, ApJ, 379, 245

Sharp, C. M. & Burrows, A. 2007, ApJS, 168, 140

Stelzer, B., Marino, A., Micela, G., López-Santiago, J., & Liefke, C. 2013, Monthly Notices of the Royal Astronomical Society, 431, 2063

van Lieshout, R., Min, M., & Dominik, C. 2014, A&A, 572, A76

van Lieshout, R., Min, M., Dominik, C., et al. 2016, A&A, 596, A32

Vanderburg, A., Johnson, J. A., Rappaport, S., et al. 2015, Nature, 526, 546

Vernet, J., Dekker, H., D'Odorico, S., et al. 2011, A&A, 536, A105

Vervack, R. J., McClintock, W. E., Killen, R. M., et al. 2010, Science, 329, 672

Willmer, C. N. A. 2018, The Astrophysical Journal Supplement Series, 236, 47